JACS
JOURNAL OF THE AMERICAN CHEMICAL SOCIETY
pubs.acs.org/JACS
Article

Selective Electrified Propylene-to-Propylene Glycol Oxidation on Activated Rh-Doped Pd

Jianan Erick Huang,[#] Yiqing Chen,[#] Pengfei Ou,[#] Xueda Ding,[#] Yu Yan, Roham Dorakhan, Yanwei Lum, Xiao-Yan Li, Yang Bai, Chengqian Wu, Mengyang Fan, Mi Gyoung Lee, Rui Kai Miao, Yanjiang Liu, Colin O'Brien, Jinqiang Zhang, Cong Tian, Yongxiang Liang, Yi Xu, Mingchuan Luo,* David Sinton, and Edward H. Sargent*

Cite This: *J. Am. Chem. Soc.* 2024, 146, 8641−8649

Read Online

ACCESS | Metrics & More | Article Recommendations | Supporting Information

ABSTRACT: Renewable-energy-powered electrosynthesis has the potential to contribute to decarbonizing the production of propylene glycol, a chemical that is used currently in the manufacture of polyesters and antifreeze and has a high carbon intensity. Unfortunately, to date, the electrooxidation of propylene under ambient conditions has suffered from a wide product distribution, leading to a low faradic efficiency toward the desired propylene glycol. We undertook mechanistic investigations and found that the reconstruction of Pd to PdO occurs, followed by hydroxide formation under anodic bias. The formation of this metastable hydroxide layer arrests the progressive dissolution of Pd in a locally acidic environment, increases the activity, and steers the reaction pathway toward propylene glycol. Rh-doped Pd further improves propylene glycol selectivity. Density functional theory (DFT) suggests that the Rh dopant lowers the energy associated with the production of the final intermediate in propylene glycol formation and renders the desorption step spontaneous, a concept consistent with experimental studies. We report a 75% faradic efficiency toward propylene glycol maintained over 100 h of operation.

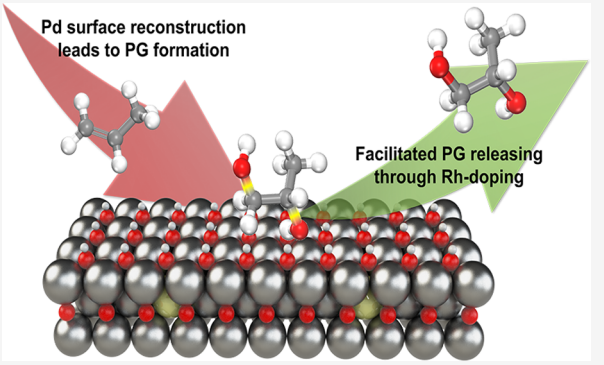

INTRODUCTION

The manufacture of commodity chemicals today relies on the combustion of fossil fuels to power thermocatalytic processes. In the United States, for example, the chemical industry consumes 28% of the total industrial energy.[1] Electrifying the chemical processes that today rely on combustion and thermocatalysis can contribute to a reduction in the carbon intensity of chemical processes. This is true with regard to the cathode, where reductive electrochemical steps such as hydrogen evolution and CO_2 reduction[2−5] have undergone continued progress, and also the anode, where one may pair selective oxidation processes.

Oxidation of olefins to epoxides and glycols is associated with a high energy demand and carbon footprint.[6] Propylene glycol (PG) represents a significant and growing market at $4B USD/year.[7] The current two-step process via propylene oxide suffers from high cost, chemical waste, and total emissions of ∼4.7 tons of CO_2 per ton of propylene glycol, one of the highest carbon intensities among commodity chemicals (Figure 1B).[8] Of these 4.7 tons, more than 3 tons of CO_2 per ton propylene glycol arise due to the propylene-to-propylene glycol step, and the rest arise from the propylene feedstock.

A chemical challenge in selectively oxidizing propylene arises from one carbon double bond and one single bond present in it, due to which, when electrooxidized, it is prone to exhibit a range of oxidation products (Figure 1A). Earlier studies on propylene oxidation in acidic media reported the oxidation of allylic carbon at a low overpotential and investigated propylene adsorption; unfortunately, these efforts, carried out on Pd,[17,31,32] led to a broad suite of partially oxidized products that include allyl alcohol, acrolein, and acrylic acid. Propylene glycol formation was also studied at a high potential under which PdO is formed,[17,28−30] but here, the FE for PG was lower than 40%, and Pd^{2+} dissolution led to acetone formation. The functionalization of the C = C double bond has been found to be more selective on Ag-based catalysts at higher overpotentials, but here, the faradic efficiency (FE) has been limited to 20%.[18] Earlier studies pointed toward the need for

Received: January 17, 2024
Revised: February 24, 2024
Accepted: February 26, 2024
Published: March 12, 2024

https://doi.org/10.1021/jacs.4c00312
J. Am. Chem. Soc. 2024, 146, 8641−8649

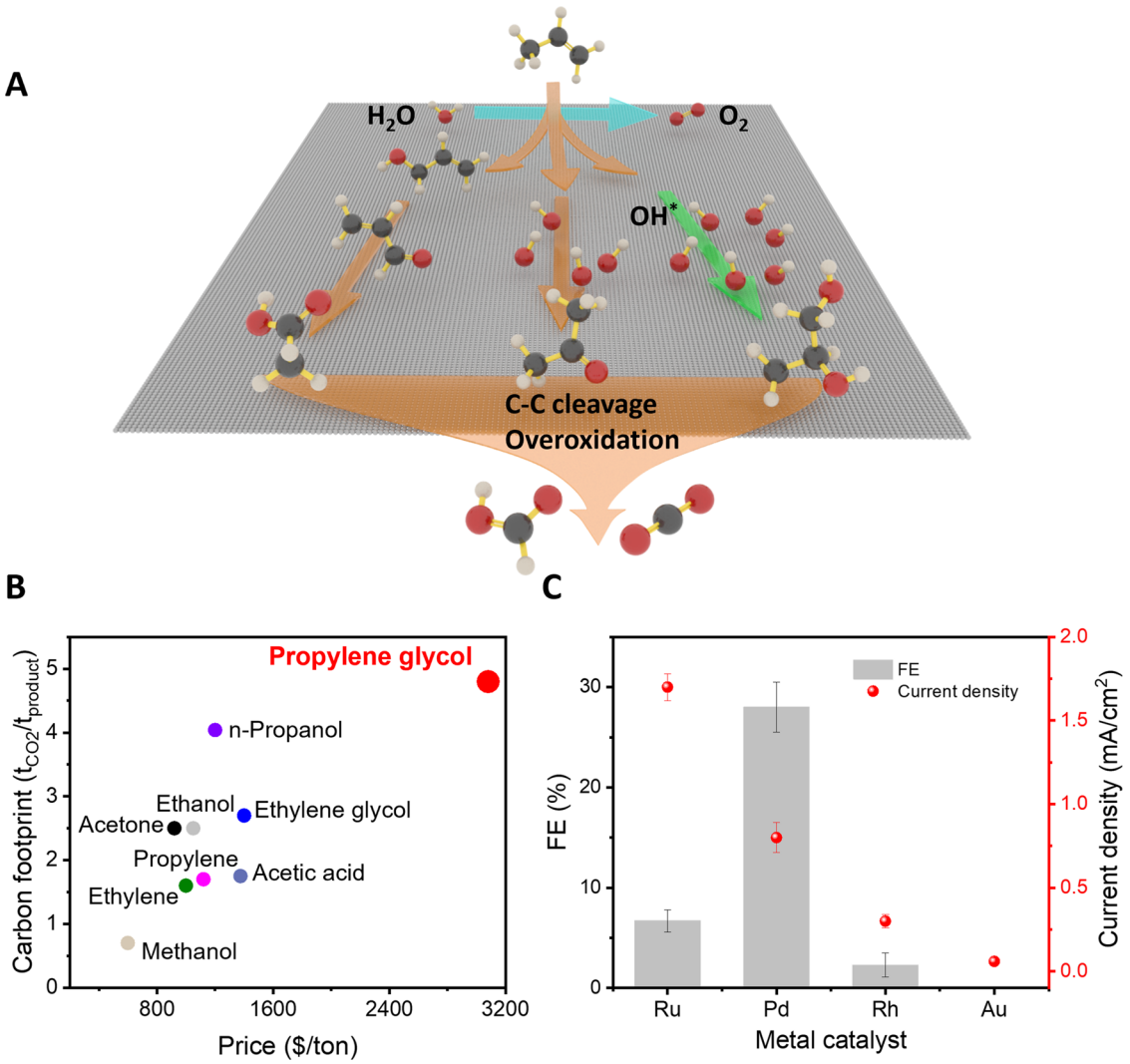

Figure 1. (A) Propylene oxidation pathways. (B) Carbon intensity vs market prices/ton of short-chain (<C_4) hydrocarbon fuels and oxygenate chemicals that have the highest global demand (≥Mt/year).[8−16] (C) Faradic efficiency (FE) toward propylene glycol and total current density of different electrodeposited noble metals.

controlled activation of the C═C double bond through the choice of catalyst and the tuning of the adsorption energies of C_3H_6 and OH on the catalyst surface.

Here, in pursuit of selective electrosynthesis of propylene glycol from propylene, we investigate how the catalyst design and activation can steer the reaction toward the desired single product, propylene glycol. Cyclic voltammetry (CV) studies, taken together with operando Raman spectroscopy, suggest that hydroxide formation on the surface of Pd and PdO during activation steers the selectivity and improves the reaction rate toward propylene glycol in near-neutral-pH electrolytes (pH 3−10), an effect that first increases and then stabilizes after a ∼2 h initial operating period. The undesired Pd dissolution that otherwise leads to acetone production is arrested by the process associated with activation, and once this hydroxide formation process is underway, propylene glycol then becomes the primary product. This metastable hydroxide layer is formed under anodic bias in a locally acidic environment and reacts with surface-adsorbed propylene via a Mars−van Krevelen-like mechanism.[29] We screened metal dopants and found that some of these (such as Sn and Ru) alter the activation process wherein Pd hydroxide is formed. Others, such as Rh, do not alter the establishment of Pd active sites and increase the selectivity toward propylene glycol (PG). Density functional theory (DFT) suggests that Rh doping reduces the energy required for $C_3H_8O_2$* formation and lowers the energetic cost of the subsequent desorption step compared to the case of pure Pd. Experimental results also show a higher partial current density and a lower concentration of the overoxidized product of propylene glycol on PdRh compared to those of pure Pd, in agreement with DFT. The best catalysts exhibit stable performance with an FE of 75% and a selectivity of over 93% in a study over 100 h of continuous operation.

RESULTS AND DISCUSSION

Propylene Oxidation as a Function of pH and Oxidizing Potential. Pd has been shown to be a good catalyst for olefin adsorption and oxidation (Figure 1C).[19,20] We used electrodeposition to form a thin layer of Pd with a nanodendritic structure (Methods section). The surface morphology of electrodeposited Pd nanodendrites was characterized using electron microscopy (Supporting Information Figures S2 and S3).

https://doi.org/10.1021/jacs.4c00312
J. Am. Chem. Soc. 2024, 146, 8641−8649

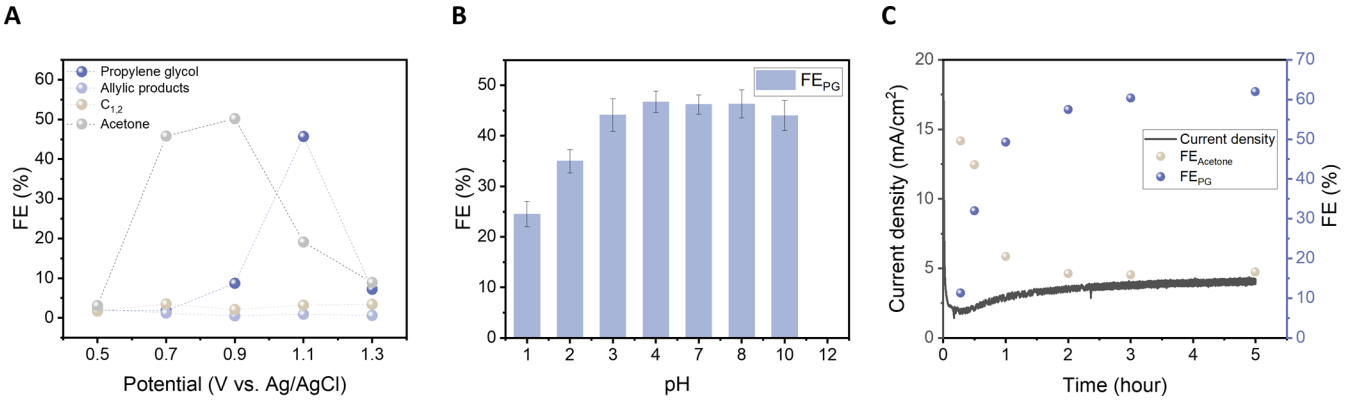

Figure 2. (A) FE of propylene oxidation vs potential in pH 4 perchlorate (0.1 M) electrolyte. The allylic product FE is very low in this electrolyte at all applied potentials. The selectivity shifts away from acetone and toward propylene glycol as we increase the potential. (B) FE of propylene glycol in different pH electrolytes under 1.1 V vs Ag/AgCl. (C) FE of acetone and propylene glycol in an extended 5 h test.

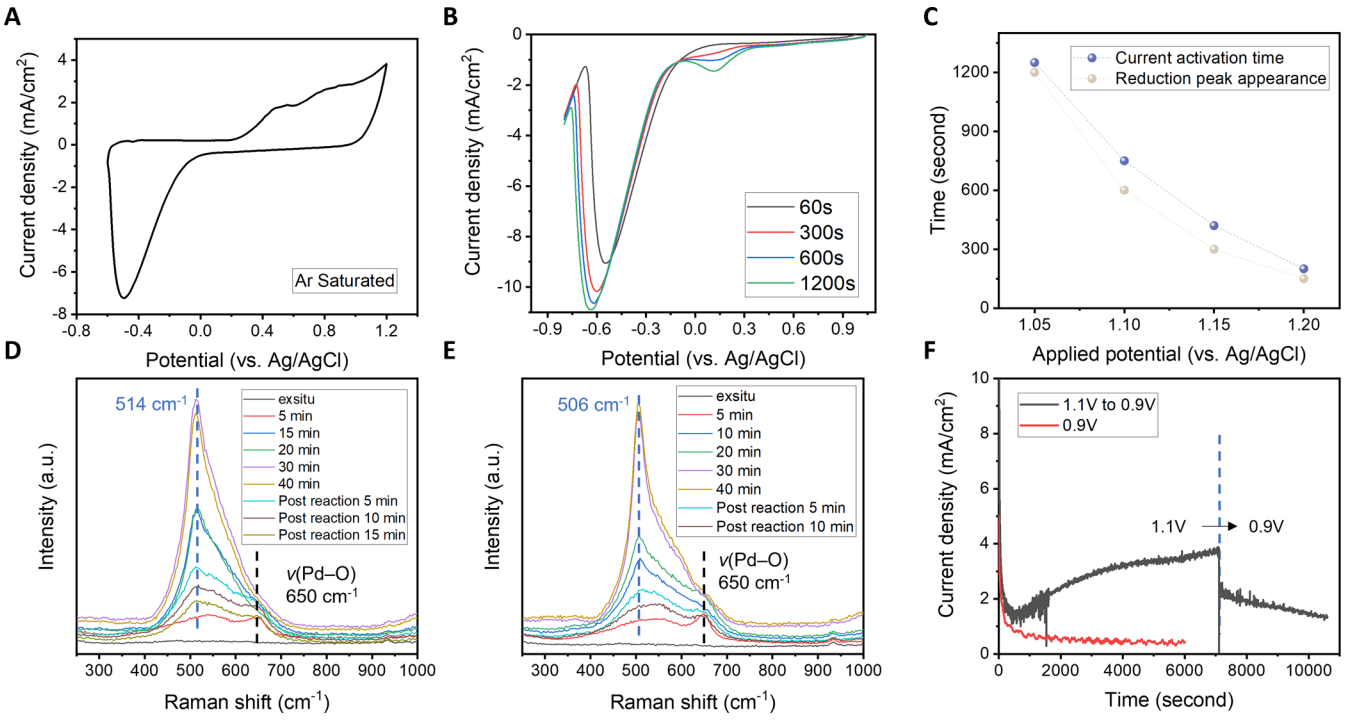

Figure 3. Mechanistic study of the causes of the temporal evolution of selectivity. (A) Cyclic voltammetry (CV) of Pd in 0.1 M $NaClO_4$ electrolyte with saturated Ar. (B) Negative scan of CV of Pd after holding at 1.1 V vs Ag/AgCl for different periods of time. (C) Comparison of the time required for current activation and the time for the appearance of a reduction peak in the CV negative scan under different anodic potentials. (D) In situ Raman of Pd in H_2O-based 0.1 M $NaClO_4$ electrolyte under 1.1 V vs Ag/AgCl. (E) In situ Raman spectra of Pd in D_2O-based 0.1 M $NaClO_4$ electrolyte under 1.1 V vs Ag/AgCl. (F) Current and FE for propylene glycol at a low potential of 0.9 V vs Ag/AgCl for activated Pd (after operating under optimal conditions for 2 h) vs the fresh Pd catalyst.

When working in 0.1 M perchloric (pH 1.1 ± 0.2) acid electrolyte (selected to avoid unwanted adsorption of anions that could block active sites[21−222324252627]), a shift in selectivity from allylic oxidized products (allyl alcohol and acrolein) to propylene glycol is observed with increasing operating potential (Figure S4), consistent with prior reports:[17] the FE for propylene glycol (FE_{PG}) reached 28% at 1.05 V vs Ag/AgCl. Acetone was observed as the main competing product, with an FE of 45%. Traces of C_1 and C_2 byproducts such as acetate and formate were detected, attributable to C−C cleavage.

Acetone has previously been reported to be a major product of homogeneous reactions involving Pd^{2+} in solution.[17,30] We checked our electrolyte and found increased Pd^{2+} concentration, presumably from the dissolution of the electrocatalyst in time (Figure S5).

We sought to prevent Pd dissolution by using a higher pH electrolyte (see the Pourbaix diagram[33]) and studying in the pH range of 3−10 (Figure 2A,B). The FE for propylene glycol reached the highest value at 1.1 V vs Ag/AgCl, and the oxygen evolution reaction (OER) became the dominant reaction when the operating potential was further increased. By sampling products in the electrolyte every 15 min, we then noticed an activation effect, i.e., a change in the product selectivity as a function of the time under operation. After the first 15 min, the current increased appreciably over the ensuing 2 h period, after

https://doi.org/10.1021/jacs.4c00312
J. Am. Chem. Soc. 2024, 146, 8641−8649

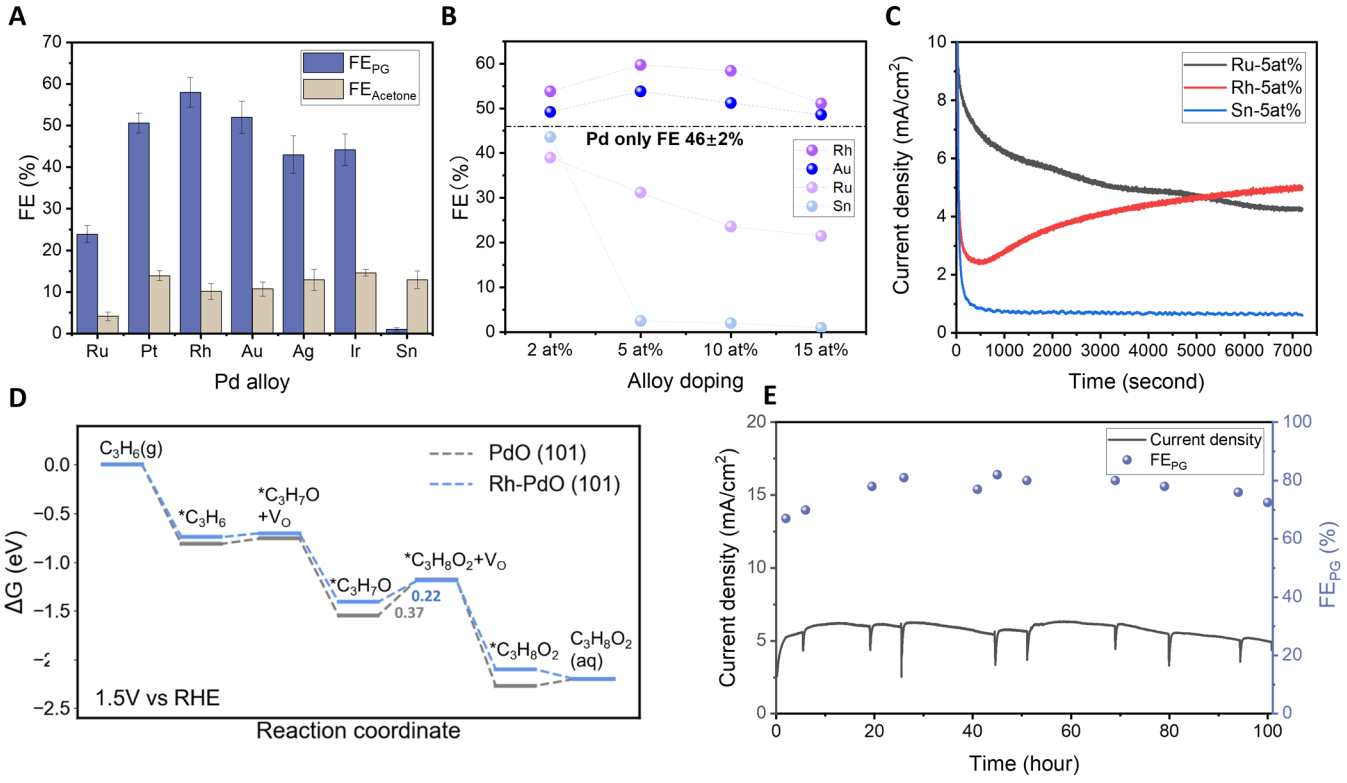

Figure 4. (A) FE for propylene glycol with seven different Pd alloys at 10 atom % doping. (B) FE for propylene glycol with PdRu, PdRh, PdAu, and PdSn alloys having different atom % of doping; the FE is calculated based on the average of a 2 h test. (C) Current profile for 5 atom %-doped Ru, Rh, and Sn in Pd catalysts at 1.1 V vs Ag/AgCl. (D) Calculated free energy diagram of propylene oxidation on PdO- and Rh-doped PdO. The introduction of lattice OH into the hydrocarbon intermediate creates a surface oxygen vacancy, which is denoted as V_O. The values in the figure indicate the free energy changes for the limiting step of the reaction. (E) Current (black) and faradic efficiency (blue) vs the time profile of a 100 h stability evaluation at 1.1 V vs Ag/AgCl with electrodeposited PdRh in pH 4 0.1 M perchlorate electrolyte; the FE is calculated between each time interval.

which the current substantially stabilized (Figure 2C). By sampling the electrolyte following the completion of the activation process, the primary product is discovered to be propylene glycol. The PG FE reached ~60% at the end of a 5 h test, and the acetone FE diminished to 15% by this point. By studying Pd^{2+} in the electrolyte, we found that its rate of dissolution had decreased significantly once the activation process had begun (Figure S6). This is in contrast to the observations made at pH 1−2, which show no activation in the current density and exhibit a progressive increase in Pd dissolution (Figure S7).

When the pH reached 12 and above, OER became the dominant process, evident from the visible bubbling on the catalyst surface and negligible propylene oxidation products. We reason that a high OH^- concentration accounts for faster OER kinetics compared to that in a neutral or slightly acidic environment, which leads to a more sluggish water dissociation process (details of the pH effect on the activation and propylene glycol selectivity are provided in the Supporting Note 1 and Figures S8−S14).

In brief, the activation phenomenon that leads to the efficient synthesis of propylene glycol is the most prominent in the pH range of 3−10, in which water dissociation remains the main OH^- source for propylene oxidation. The activation of the catalyst increases the propylene oxidation to propylene glycol to an FE of ~60%. In contrast, the continuous Pd dissolution in the pH 1−2 electrolyte impedes the catalyst activation process, and the FE_{PG} is consistently below 40%, while the OER dominates at bulk pH > 11 due to abundant OH^-.

Propylene Oxidation Activation on Pd. Cyclic voltammetry was performed to investigate the species present following the observation of activation. CV (carried out in an Ar-saturated electrolyte) before activation shows the oxidation and reduction peaks corresponding to the interconversion between metallic Pd and PdO (Figure 3A).[34] We operated the catalyst at a constant oxidative potential of 1.1 V vs Ag/AgCl for durations lasting between 1 and 20 min and then carried out negative CV scans to identify other possible oxides in addition to the typical PdO. A new feature at 0.1 V vs Ag/AgCl emerged after operating for about 10 min (Figure 3B), roughly the same time as that on which the activation process occurs. This study was then repeated with a range of applied potentials used in the activation process and found a good correlation (Figures 3C and S15) between the activation time and the time of onset of the reduction peak at 0.1 V. We then compared the influence of running the activation process in the presence of Ar vs propylene and found no influence on the emergence of this 0.1 V feature from the choice of gas in the headspace (Figure S16).

Using operando Raman under an applied potential of 1.1 V, we found that the feature at 650 cm^{-1} (previously reported to be ν(PdO))[35] grows quickly (within 5 min) and stabilizes. Over the activation period of 10−40 min, a new feature at 514 cm^{-1} grows progressively (Figure 3D). To test whether this feature includes an effect of the hydroxide or oxygen in water,

https://doi.org/10.1021/jacs.4c00312
J. Am. Chem. Soc. 2024, 146, 8641−8649

we replaced H_2O with D_2O and repeated the Raman study (Figure 3E). A red shift to 506 cm^{-1} was observed while the characteristic peak of ν(PdO) remained the same at 650 cm^{-1}. This suggests that the 514 cm^{-1} feature is linked to ν(Pd−OH) as the Pd−OH bond is expected to vibrate at a slightly lower frequency than the Pd−OH bond. Subsequent ex situ post-reaction spectra showed that this 514 cm^{-1} peak diminished progressively once we removed the applied oxidizing potential. We interpret this to mean that the surface reverts to PdO. This is consistent with our CV negative scan results, where a similar loss in the 0.1 V feature is observed when the catalyst is left in an open circuit (Figure S17). These findings suggest that the catalytically active surface hydroxide is stable under anodic bias but gradually reverts when the bias is removed.

Pd is a non-surface-enhanced Raman scattering (SERS) material, so the feature associated with Pd−OH is likely not localized to a single monolayer surface but instead is a layer of hydroxide material that grows into the catalyst from the electrolyte over the course of the activation period. Post-reaction X-ray diffraction (XRD) shows a shift to a lower angle in the diffraction pattern following anodic bias in solution over a 20 min time course (Figure S18). The delay between the removal of the anodically biased catalyst sample from the electrolyte and the completion of the acquisition of X-ray data for XRD was approximately 5 min, which is before the active species completely reverted to Pd and PdO. The XRD results showed a left shift in the diffraction patterns of Pd over the first 20 min, which slowly stabilized after 1 h, suggesting increasing distance between the atomic layers due to the formation of the hydroxide.

To study the conditions for generating and consuming the hydroxide, we carried out propylene oxidation at 1.1 V vs Ag/AgCl for 2 h by fully activating it and found that when the applied bias was lowered to 0.9 V, the faradic efficiency for PG remained at ∼40% over the ensuing hour (Figure 3F). In contrast, if the catalyst is prepared by operating at the same applied bias of 0.9 V, it fails to activate in the first 2 h, providing an FE_{PG} less than 10%. In the first study, when we lowered the bias from 1.1 to 0.9 V, the current decayed with time over the course of an hour to 0.9 V, indicating a continuous loss of the hydroxide species: we propose that the hydroxide is no longer efficiently replenished, and it progressively diminishes as it is consumed to form propylene glycol from propylene.

Improving Propylene Glycol Performance using Metal Dopants. Seeking further improvements in the selective oxidation of propylene to propylene glycol, we screened a series of metal dopants including Ru, Au, Ag, Pt, Rh, Ir, and Sn. We studied the impact on FE_{PG} (Figure 4A) following a common 2 h activation period of alloys and found that both Rh- and Au-doped Pd showed improved FE, while Ru- and Sn-doped Pd had a much lower FE_{PG}. We optimized the dopant concentration and found 5 atom % to be optimal for both Rh and Au (Figure 4B). X-ray photoelectron spectroscopy (XPS), inductively coupled plasma optical emission spectroscopy (ICP-OES) (Figure S19 and Table S2), and XRD indicate that the dopants were incorporated and did not cause phase segregation (Figure S20).

We found that the FE-improving dopants (Rh and Au) showed the reported activation effect, and the FE-diminishing dopants (Ru, Sn) showed no activation (Figure 4C). Based on the much higher and lower current densities in Ru- and Sn-doped Pd respectively, we propose that Ru leads to a high rate of OER and does not produce the activated Pd−OH species. Sn results in a very slow OH generation.

To better understand the effect of these dopants on propylene glycol production, we further investigated, using the CV negative scan method, their influence on the formation of Pd active sites. Upon comparing the reduction peaks across PdRu, PdSn, PdRh, and Pd after 1200 s at 1.1 V vs Ag/AgCl, we found that the peaks for PdRh and Pd are significantly larger than those for PdSn and PdRu (Figure S21). This suggests differing degrees of hydroxide formation among these samples, likely influenced by the distinct water oxidation capabilities of the dopants. A constant potential test at 1.1 V vs Ag/AgCl is then performed in an Ar-saturated electrolyte for approximately 20 min, followed by the introduction of propylene. The changes were monitored with respect to the current density and the FE was measured for the ensuing 20 min (Figure S22). PdRu has the highest current density in the Ar-saturated electrolyte, with much higher O_2 detected at the gas outlet than the other three catalysts, indicating faster OER kinetics. Both Pd and PdRh demonstrated a nearly 2-fold increase in the current density, with PdRh exhibiting an increase in the FE for propylene glycol from 61% (in the case of Pd) to 71% (in the case of PdRh). PdSn caused negligible change and kept decaying upon the introduction of propylene, with acetone as the main product; the current was therefore assigned to the dissolution of Pd and slow surface oxidation that kept decreasing over time.

As the Rh dopant did not increase the activation signal seen in CV following activation, and the electrochemical surface area does not show an obvious change before and after the activation for both Pd and PdRh (Figure S23 and Table S1), we sought further indicators as to the cause of the increased selectivity to PG. DFT was applied to identify intermediates and energetic steps along the reaction pathway, and for this, we assumed a Mars−van Krevelen-like (MvK) mechanism involved in the adsorption of propylene, the introduction of lattice OH (on the surface of the Pd/PdRh catalyst) into the hydrocarbon intermediate, the regeneration of lattice OH, and the desorption of propylene glycol (Figures 4D, S24, and S25). We found that introducing Rh causes the desorption of $C_3H_8O_2$ to become spontaneous in the final step of the reaction pathway, in contrast to the barrier when pure Pd is used. To analyze the DFT results, we compared the FE for other products in the cases of Pd vs PdRh. Acetate, formate, acetaldehyde, and lactic acid are the main overoxidized liquid products, with only traces of CO_2. PdRh shows a higher partial current density and lower overoxidized product concentration at potentials from 1.05 to 1.2 V vs Ag/AgCl (Figure S26), in agreement with the DFT predictions.

We examined the stability in the highest-performing catalyst, PdRh-5 atom %, operating over 100 h at 1.5 V vs reversible hydrogen electrode (RHE) (Figure 4E). We associate the slightly decaying current density and FE after long periods of operation with the continuously decreasing pH and an increased concentration of propylene glycol and overoxidized products in the anolyte (Figure S27, Table S3). When portions of the electrolyte were replaced with fresh electrolyte every 10−20 h to limit the concentration of liquid products, we found that the FE was stabilized at 75% for propylene glycol at around 5 mA/cm^2, with a selectivity (the rate of propylene glycol formation relative to total oxidized propylene products) asymptoting to 93%.

https://doi.org/10.1021/jacs.4c00312
J. Am. Chem. Soc. 2024, 146, 8641−8649

CONCLUSIONS

We report the direct electrochemical production of propylene glycol, a commodity chemical having a high carbon intensity today. Reconstruction of near-surface Pd under an anodic potential at pH 3−10 enables an increase in the selectivity toward propylene glycol. We suggest that metal hydroxide stabilized by an applied anodic potential provides catalytic activity. Rh-doped Pd reduced the energy required for propylene glycol formation and desorption and led to 75% FE for propylene glycol without decay over 100 h of operation. The metastable hydroxide phase that enhances the propylene glycol selectivity can potentially be further developed and applied in other hydrocarbon oxidation reactions. By studying the interplay of pH and potential on catalyst activation and the dopant effect, it may be possible to develop additional catalysts whose active sites are stable on a high-surface-area substrate, ideally one that operates on a gas diffusion electrode to enable higher current densities. The conversion of propylene to propylene glycol at the anode is an example of a reaction that can be paired with cathodic processes to increase the efficient utilization of scarce low-carbon electricity from both economic and carbon-intensity viewpoints.

METHODS

Materials. All chemicals used here, including potassium hexachloropalladate, potassium hexachloroplatinate, rhodium nitrate solution, sodium hexachloroiridate, ruthenium chloride hydrates, gold chloride, silver nitrate, tin chloride, palladium oxide particles, sodium perchlorate, and perchloric acid, are purchased from Sigma-Aldrich. The Nafion 117 membrane, Pd foil, and Pt mesh are purchased from the Fuel Cell store. Deionized (DI) water (18.2 MΩ) was used for all of the electrolyte preparations. The N_2 gas and propylene gas cylinders are purchased from Linde gas.

Catalyst Synthesis. The pure Pd sample was prepared using electrochemical deposition technique in a solution consisting of 2 mM K_2PdCl_6 and 0.5 M H_2SO_4 with stirring. The electrolytic cell used for electrodeposition consisted of a 3-mm-diameter glassy carbon working electrode (used as the substrate for electrodeposition), a 2 cm × 2 cm Pd foil counter electrode, and an Ag/AgCl (3 M KCl) reference electrode. The stir rate was kept constant at 1200 rpm throughout the reaction. The Pd alloy samples, Pd−Rh, Pd−Pt, Pd−Ru, Pd−Ir, Pd−Ag, Pd−Au and Pd−Sn, are prepared with the addition of $Rh(NO_3)_3$, K_2PtCl_6, $RuCl_3$, Na_2IrCl_6, $Ag(NO)_3$, $AuCl_2$, and $SnCl_2$ in the original precursor solution. The four different alloy precursors were prepared by adding each metal salt, $Rh(NO_3)_3$, $RuCl_3$, $AuCl_3$, and $SnCl_2$, into the Pd electrodeposition precursors to synthesize 2, 5, 10, and 15 atom % final solutions, respectively. The electrodeposition was operated under −1 V vs Ag/AgCl for a duration of 15 min. The sample was then taken out, washed with DI water, and dried with nitrogen before any further tests. The pure Ru, Rh, and Au samples were prepared using the same electrochemical deposition technique as the pure Pd sample, but with 2 mM $RuCl_3$, $Rh(NO_3)_3$, and $AuCl_2$ respectively.

Electrochemical Measurement. All electrochemical measurements were performed using an electrochemical station (Autolab PGSTATS204) and carried out in a glass H-cell with a 3-electrode setup: electrodeposited Pd-based catalyst on a glassy carbon working electrode, a Pt foil counter electrode, and an Ag/AgCl (3 M KCl) reference electrode. A Nafion 117 membrane was used to separate the anode and cathode chambers. The electrolytes used for the test were 0.1 M perchlorate aqueous solution with a volume of 25 mL in both the anode and cathode chambers. The pH was adjusted with the amount of perchloric acid in the electrolyte. Propylene was bubbled into the anode chamber continuously at a rate of around 15−20 sccm. All tests start after propylene bubbling for 5 min to reach saturation.

The propylene oxidation performances were tested in this h-cell setup under potentiostatic mode. A stir bar was placed in the anolyte chamber below the working electrode, and the stir rate was kept constant at 1200 rpm during the constant voltage tests. All of the tests were not *iR* compensated. 1 mL aliquots of the electrolyte were subjected to NMR spectroscopy for product characterization during the tests, and the same amount of fresh electrolyte was replenished.

Cyclic voltammetry (CV) was performed in the same h-cell setup that was used for performance evaluation and saturated with either nitrogen or propylene through continuous bubbling. Electrodeposited Pd, Ag/AgCl (3 M KCl), and Pt mesh were used as the working, reference, and counter electrodes, respectively. Perchloric acid and potassium perchlorate are used to adjust the pH of the electrolyte, with the total perchlorate concentration controlled at 0.1 M. The scan rate was kept constant at 20 mV/s. A Nafion 117 membrane was used to separate the anode and cathode chambers. The current−voltage profile was not *iR* compensated. All potentials were converted to the RHE scale via the following equation

$$E\ (\mathrm{RHE}) = E\ (\mathrm{Ag/AgCl}) + 0.059 \times \mathrm{pH} + 0.197$$

Material Characterizations. The electrodeposited Pd was characterized by scanning electron microscopy (Hitachi S-5200) and transmission electron microscopy (FEI Titan 80-300 LB). The PdSn, PdRu, and PdRh alloy compositions were tested using ICP-OES (Agilent 700). X-ray photoelectron spectroscopy (XPS) was carried out in an electron spectroscopy for chemical analysis (ESCA) device (PHI 5700) with Al Kα X-ray energy source (1486.6 eV) for excitation. XRD patterns were obtained by a benchtop X-ray diffractometer (Miniflex, Rigaku). Raman tests are carried out using a Renishaw inVia Raman Microscope and an in situ lens with a water immersion objective (HCX APO L 63x/0.90 W UV Immersion). A custom-made cell was used to carry out in situ Raman spectroscopy. A laser wavelength of 532 nm was used as the excitation source. The laser power was kept lower than 0.20 mW in all experiments to minimize sample damage. A Raman spectrometer was calibrated with Si. The alloy composition was determined via ICP-OES on an Agilent 700 Series ICP-OES spectrometer operating in axial mode. ICP samples were prepared by dissolution in diluted aqua regia solution.

^{1}H NMR spectroscopy (600 MHz Agilent DD2 NMR Spectrometer) was performed to measure the content of propylene glycol in the final electrolyte. Dimethyl sulfoxide was used as the reference standard for quantifying the product, and D_2O was used as the solvent for the product. The faradic efficiency was calculated using the equation below:

$$\text{faradaic efficiency}\ (\%) = N \times F \times = n_{\mathrm{product}}/Q$$

where N is the number of electrons transferred, F is the faradic constant, n_{product} is the total moles of products, and $Q = i \times t$ is the total charge passed during the experiment.

Reference standard solution: 35 mg of DMSO is first mixed with 5500 mg of D_2O (solution 1). Solution 1 is then further diluted, and 120 mg of solution 1 is mixed with 7800 mg of D_2O, which is the final reference standard solution. The exact weight of each chemical mentioned above might vary among different batches. In the final samples that are used for the NMR test, 100 μL of the reference standard solution is added into 600 μL of the final electrolyte, and the final concentration of DMSO in the solution is in the ppm level (3−5 ppm). Based on the area ratio between DMSO and propylene glycol peak, we are able to calculate the values of n_{product} and FE. An example of the spectrum is provided in the Supporting Information Figure S29.

Energy Efficiency Calculation. The energy analysis is carried out on propylene oxidation on an anode coupled with the hydrogen evolution reaction on the cathode. For each ton of propylene glycol produced at the anode, 0.046 tons of hydrogen are also produced at the cathode. We calculate the electricity cost to produce each ton of propylene glycol as follows

$$\begin{aligned}&\text{energy cost (GJ/ton)}\\ &\quad = 1000000/(62\ \mathrm{g/mol}) \times 96485\ \mathrm{C/mol} \times 2/\mathrm{FE}\\ &\qquad \times \text{voltage}/1000000000\end{aligned}$$

https://doi.org/10.1021/jacs.4c00312
J. Am. Chem. Soc. 2024, 146, 8641−8649

At a full cell of 2 V and 75% FE for propylene glycol, the electricity energy cost per ton of propylene glycol produced is around 8 GJ, a reaction also accompanied by the generation of 0.046 tons of hydrogen, which corresponds to 5.6 GJ using a higher heating value (HHV) of 120 GJ/ton.

Computational Studies. Spin-polarized density functional theory (DFT)[36] was performed using the Vienna Ab Initio Simulation Package (VASP).[37,38] The Perdew−Burke−Ernzerhof (PBE) functional was used to represent the exchange−correlation of the Kohn−Sham equation,[39,40] and the projector-augmented wave (PAW) approach was utilized to describe the electron−ion interactions.[41] Grimme's DFT-D3 method was employed to include long-range dispersion interactions.[42,43] The implicit solvent model was used to consider the solvent effect as implemented in VASPsol.[44] The kinetic energy cutoff was set to 450 eV, and the Brillouin zone was sampled by a 2 × 2 × 1 Mokhorst−Pack *k*-point grid.[45] Structures were relaxed until residual forces were less than 0.02 eV/Å and the energy difference was smaller than 10^{-5} eV.

We selected a stoichiometric PdO(101) slab model to represent the oxidized Pd surface, as PdO(101) is the most commonly observed oxide surface on Pd(111) and exhibits higher activity compared to the PdO(100) and Pd(110) surfaces.[46−49] A four-layered supercell with 64 Pd and 64 O atoms was constructed, with the atoms in the bottom two layers fixed in their bulk positions. For the Rh-doped PdO(101), we examined two potential substitutional positions: surface and subsurface. We determined that the subsurface position is thermodynamically favorable and utilized it for subsequent adsorption calculations. To account for the surface hydroxyls observed in the experiment, we fully saturated the surface oxygen atoms of PdO(101) and Rh-PdO(101) with hydrogen atoms, creating a layer of lattice OH. For all slabs, a vacuum spacing of at least 15 Å along the normal direction to the surface was set to avoid image interaction.

Chemical Commodity Prices. All data related to the chemical commodity prices and carbon footprint are acquired in the reference literature and collaboration partners. Most of the chemical commodity prices are taken with reference to the chemanalyst Web site via doi: https://www.chemanalyst.com/Pricing/Pricingoverview

■ ASSOCIATED CONTENT

Supporting Information

The Supporting Information is available free of charge at https://pubs.acs.org/doi/10.1021/jacs.4c00312.

> Schematic of the full-cell reaction that simultaneously upgrades the feedstock at both the cathode and the anode; transmission electron micrograph of electrodeposited Pd; acetone FE and Pd concentration in 0.1 M perchlorate electrolyte (pH 7) under 1.1 V vs Ag/AgCl; comparison of the propylene glycol FE of the Pd catalyst under different operating potentials in the electrolyte of different pH values; comparison of the ECSA of Pd and PdRh catalyst before and after activation performed through a CO stripping test; composition of Pd alloy catalysts measured by ICP-OES, XPS and XRD; CV scans of Pd catalyst after operating under different potentials for different time duration; CV scans of Pd alloy after operating under 1.1 V vs Ag/AgCl for different time duration (PDF)

■ AUTHOR INFORMATION

Corresponding Authors

Mingchuan Luo − *School of Material Science and Engineering, Peking University, Beijing 100871, China*; Email: m.luo@pku.edu.cn

Edward H. Sargent − *Department of Electrical and Computer Engineering, University of Toronto, Toronto, Ontario M5S 1A4, Canada*; orcid.org/0000-0003-0396-6495; Email: ted.sargent@utoronto.ca

Authors

Jianan Erick Huang − *Department of Electrical and Computer Engineering, University of Toronto, Toronto, Ontario M5S 1A4, Canada*; orcid.org/0000-0001-5872-3680

Yiqing Chen − *Department of Electrical and Computer Engineering, University of Toronto, Toronto, Ontario M5S 1A4, Canada*; orcid.org/0000-0002-2686-5593

Pengfei Ou − *Department of Electrical and Computer Engineering, University of Toronto, Toronto, Ontario M5S 1A4, Canada*; orcid.org/0000-0002-3630-0385

Xueda Ding − *School of Material Science and Engineering, Peking University, Beijing 100871, China*

Yu Yan − *Department of Electrical and Computer Engineering, University of Toronto, Toronto, Ontario M5S 1A4, Canada*

Roham Dorakhan − *Department of Electrical and Computer Engineering, University of Toronto, Toronto, Ontario M5S 1A4, Canada*

Yanwei Lum − *Institute of Materials Research and Engineering, Agency for Science, Technology and Research (A*STAR), Singapore 138634, Singapore*

Xiao-Yan Li − *Department of Electrical and Computer Engineering, University of Toronto, Toronto, Ontario M5S 1A4, Canada*; orcid.org/0009-0003-2325-7538

Yang Bai − *Department of Electrical and Computer Engineering, University of Toronto, Toronto, Ontario M5S 1A4, Canada*; orcid.org/0000-0002-1643-3770

Chengqian Wu − *Department of Mechanical and Industrial Engineering, University of Toronto, Toronto, Ontario M5S 3G8, Canada*

Mengyang Fan − *Department of Mechanical and Industrial Engineering, University of Toronto, Toronto, Ontario M5S 3G8, Canada*

Mi Gyoung Lee − *Department of Materials Science and Engineering, Incheon National University, Incheon 22012, Republic of Korea*

Rui Kai Miao − *Department of Mechanical and Industrial Engineering, University of Toronto, Toronto, Ontario M5S 3G8, Canada*

Yanjiang Liu − *Department of Electrical and Computer Engineering, University of Toronto, Toronto, Ontario M5S 1A4, Canada*; orcid.org/0000-0002-6119-2793

Colin O'Brien − *Department of Mechanical and Industrial Engineering, University of Toronto, Toronto, Ontario M5S 3G8, Canada*

Jinqiang Zhang − *Department of Electrical and Computer Engineering, University of Toronto, Toronto, Ontario M5S 1A4, Canada*; orcid.org/0000-0001-5476-0134

Cong Tian − *Department of Electrical and Computer Engineering, University of Toronto, Toronto, Ontario M5S 1A4, Canada*

Yongxiang Liang − *Department of Electrical and Computer Engineering, University of Toronto, Toronto, Ontario M5S 1A4, Canada*

Yi Xu − *Department of Mechanical and Industrial Engineering, University of Toronto, Toronto, Ontario M5S 3G8, Canada*

David Sinton − *Department of Mechanical and Industrial Engineering, University of Toronto, Toronto, Ontario M5S 3G8, Canada*; orcid.org/0000-0003-2714-6408

Complete contact information is available at: https://pubs.acs.org/10.1021/jacs.4c00312

Author Contributions

[#]J.E.H., Y.C., P.O., and X.D. contributed equally to this work.

Notes

The authors declare no competing financial interest.

■ ACKNOWLEDGMENTS

The authors acknowledge support from the Ontario Research Fund-Research Excellence Program, the National Research Council (NRC), the Canada Research Chairs program, and the Natural Sciences and Engineering Research Council (NSERC).

■ REFERENCES

(1) U.S. Energy Information Administration. *Use of Energy Explained*, 2019.
(2) Ayers, K.; Danilovic, N.; Ouimet, R.; et al. Perspectives on Low-Temperature Electrolysis and Potential for Renewable Hydrogen at Scale. *Annu. Rev. Chem. Biomol. Eng.* **2019**, *10*, 219−239.
(3) Birdja, Y. Y.; Pérez-Gallent, E.; Figueiredo, M. C.; et al. Advances and challenges in understanding the electrocatalytic conversion of carbon dioxide to fuels. *Nat. Energy* **2019**, *4*, 732−745.
(4) Ozden, A.; García de Arquer, F. P.; Huang, J. E.; et al. Carbon-efficient carbon dioxide electrolysers. *Nat. Sustainability* **2022**, *5*, 563−573.
(5) Vesborg, P. C. K.; Seger, B.; Chorkendorff, I. Recent Development in Hydrogen Evolution Reaction Catalysts and Their Practical Implementation. *J. Phys. Chem. Lett.* **2015**, *6*, 951−957.
(6) *Technology Roadmap - Energy and GHG Reductions in the Chemical Industry via Catalytic Processes*, 2013.
(7) Yan, M.; Kawamata, Y.; Baran, P. S. Synthetic Organic Electrochemical Methods Since 2000: On the Verge of a Renaissance. *Chem. Rev.* **2017**, *117*, 13230−13319.
(8) Bartolini, N.; Casasso, A.; Bianco, C.; Sethi, R. Environmental and Economic Impact of the Antifreeze Agents in Geothermal Heat Exchangers. *Energies* **2020**, *13*, No. 5653.
(9) Nitopi, S.; Bertheussen, E.; Scott, S. B.; et al. Progress and Perspectives of Electrochemical CO2 Reduction on Copper in Aqueous Electrolyte. *Chem. Rev.* **2019**, *119*, 7610−7672.
(10) Kibria, M. G.; Edwards, J. P.; Gabardo, C. M.; et al. Electrochemical CO2 Reduction into Chemical Feedstocks: From Mechanistic Electrocatalysis Models to System Design. *Adv. Mater.* **2019**, *31*, No. 1807166.
(11) Artz, J.; Müller, T. E.; Thenert, K.; et al. Sustainable Conversion of Carbon Dioxide: An Integrated Review of Catalysis and Life Cycle Assessment. *Chem. Rev.* **2018**, *118*, 434−504.
(12) Jouny, M.; Hutchings, G. S.; Jiao, F. Carbon monoxide electroreduction as an emerging platform for carbon utilization. *Nat. Catal* **2019**, *2*, 1062−1070.
(13) Kibria Nabil, S.; McCoy, S.; Kibria, M. G. Comparative life cycle assessment of electrochemical upgrading of CO2 to fuels and feedstocks. *Green Chem.* **2021**, *23*, 867−880.
(14) Lark, T. J.; Hendricks, N. P.; Smith, A.; et al. Environmental outcomes of the US Renewable Fuel Standard. *Proc. Natl. Acad. Sci. U.S.A.* **2022**, *119*, No. e2101084119.
(15) Nijhuis, T. A.; Makkee, M.; Moulijn, J. A.; Weckhuysen, B. M. The production of propene oxide: Catalytic processes and recent developments. *Ind. Eng. Chem. Res.* **2006**, *45*, 3447−3459.
(16) Liew, F. E.; Nogle, R.; Abdalla, T.; et al. Carbon-negative production of acetone and isopropanol by gas fermentation at industrial pilot scale. *Nat. Biotechnol.* **2022**, *40*, 335−344.
(17) Winiwarter, A.; Silvioli, L.; Scott, S. B.; et al. Towards an atomistic understanding of electrocatalytic partial hydrocarbon oxidation: propene on palladium. *Energ Environ. Sci.* **2019**, *12*, 1055−1067.
(18) Ke, J. W.; Zhao, J.; Chi, M.; et al. Facet-dependent electrooxidation of propylene into propylene oxide over Ag3PO4 crystals. *Nat. Commun.* **2022**, *13*, No. 932.
(19) Weixing, W.; Wang, Y. Electrochemical oxidation of ethylene on Palladium Electrode. *J. Electrochem.* **2022**, No. 2215004.
(20) Lum, Y.; Huang, J. E.; Wang, Z.; et al. Tuning OH binding energy enables selective electrochemical oxidation of ethylene to ethylene glycol. *Nat. Catal.* **2020**, *3*, 14−22.
(21) Kamat, G. A.; Zamora Zeledón, J. A.; Gunasooriya, G. T. K. K.; et al. Acid anion electrolyte effects on platinum for oxygen and hydrogen electrocatalysis. *Commun. Chem.* **2022**, *5*, No. 20.
(22) Nagao, R.; Cantane, D. A.; Lima, F. H. B.; Varela, H. Influence of Anion Adsorption on the Parallel Reaction Pathways in the Oscillatory Electro-oxidation of Methanol. *J. Phys. Chem. C* **2013**, *117*, 15098−15105.
(23) Tao, H. B.; Xu, Y.; Huang, X.; et al. A General Method to Probe Oxygen Evolution Intermediates at Operating Conditions. *Joule* **2019**, *3*, 1498−1509.
(24) Xiang, C. X.; Papadantonakis, K. M.; Lewis, N. S. Principles and implementations of electrolysis systems for water splitting. *Mater. Horiz* **2016**, *3*, 169−173.
(25) Giordano, L.; Han, B.; Risch, M.; et al. pH dependence of OER activity of oxides: Current and future perspectives. *Catal. Today* **2016**, *262*, 2−10.
(26) Huang, Y. F.; Kooyman, P. J.; Koper, M. T. M. Intermediate stages of electrochemical oxidation of single-crystalline platinum revealed by in situ Raman spectroscopy. *Nat. Commun.* **2016**, *7*, No. 12440.
(27) Lin, C.; et al. In-situ reconstructed Ru atom array on alpha-MnO2 with enhanced performance for acidic water oxidation. *Nat. Catal.* **2021**, *4*, 1012−1023.
(28) Koroidov, S.; Winiwarter, A.; Diaz-Morales, O.; et al. Chemisorbed oxygen or surface oxides steer the selectivity in Pd electrocatalytic propene oxidation observed by operando Pd L-edge X-ray absorption spectroscopy. *Catal. Sci. Technol.* **2021**, *11*, 3347−3352.
(29) Liu, X.-C.; Wang, T.; Zhang, Z. M.; et al. Reaction Mechanism and Selectivity Tuning of Propene Oxidation at the Electrochemical Interface. *J. Am. Chem. Soc.* **2022**, *144* (45), 20895−20902.
(30) Jong, R. P. H.; Dubbelman, E.; Mul, G. Electro-oxidation of propylene by palladium functionalized titanium hollow fibre electrodes. *J. Catal.* **2022**, *416*, 18−28.
(31) Winiwarter, A.; Boyd, M. J.; Scott, S. B.; et al. CO as a Probe Molecule to Study Surface Adsorbates during Electrochemical Oxidation of Propene. *ChemElectroChem* **2021**, *8*, 250−256.
(32) Silvioli, L.; Winiwarter, A.; Scott, S. B.; et al. Rational Catalyst Design for Higher Propene Partial Electro-oxidation Activity by Alloying Pd with Au. *J. Phys. Chem. C* **2022**, *126* (34), 14487−14499.
(33) Lyon, S. Corrosion of Noble Metals. *Shreir's Corrosion* **2010**, 2205−2223.
(34) Grden, M.; et al. Electrochemical behaviour of palladium electrode: Oxidation, electrodissolution and ionic adsorption. *Electrochim. Acta* **2018**, *26*, 7583−7598.
(35) Kumari, T.; Gopal, R.; et al. Sol−Gel Synthesis of Pd@PdO Core−Shell Nanoparticles and Effect of Precursor Chemistry on Their Structural and Optical Properties. *J. Inorg. Organomet. Polym. Mater.* **2019**, *29*, 316−325.
(36) Kohn, W.; Sham, L. J. Self-Consistent Equations Including Exchange and Correlation Effects. *Phys. Rev.* **1965**, *140* (4A), A1133−A1138.
(37) Kresse, G.; Joubert, D. From ultrasoft pseudopotentials to the projector augmented-wave method. *Phys. Rev. B* **1999**, *59* (3), 1758−1775.
(38) Kresse, G.; Furthmüller, J. Efficient iterative schemes for ab initio total-energy calculations using a plane-wave basis set. *Phys. Rev. B* **1996**, *54* (16), 11169−11186.
(39) Perdew, J. P.; Burke, K.; Ernzerhof, M. Generalized Gradient Approximation Made Simple. *Phys. Rev. Lett.* **1996**, *77* (18), 3865−3868.
(40) Perdew, J. P.; Chevary, J. A.; Vosko, S. H.; Jackson, K. A.; Pederson, M. R.; Singh, D. J.; Fiolhais, C. Atoms, molecules, solids,

https://doi.org/10.1021/jacs.4c00312
J. Am. Chem. Soc. 2024, 146, 8641−8649

and surfaces: Applications of the generalized gradient approximation for exchange and correlation. *Phys. Rev. B* **1992**, *46* (11), 6671−6687.
(41) Blöchl, P. E. Projector augmented-wave method. *Phys. Rev. B* **1994**, *50* (24), 17953−17979.
(42) Grimme, S.; Antony, J.; Ehrlich, S.; Krieg, H. A consistent and accurate ab initio parametrization of density functional dispersion correction (DFT-D) for the 94 elements H-Pu. *J. Chem. Phys.* **2010**, *132* (15), No. 154104.
(43) Grimme, S.; Ehrlich, S.; Goerigk, L. Effect of the damping function in dispersion corrected density functional theory. *J. Comput. Chem.* **2011**, *32* (7), 1456−1465.
(44) Mathew, K.; Sundararaman, R.; Letchworth-Weaver, K.; Arias, T.; Hennig, R. G. Implicit solvation model for density-functional study of nanocrystal surfaces and reaction pathways. *J. Chem. Phys.* **2014**, *140* (8), No. 084106.
(45) Monkhorst, H. J.; Pack, J. D. Special points for Brillouin-zone integrations. *Phys. Rev. B* **1976**, *13* (12), 5188.
(46) Weaver, J. F.; Devarajan, S. P.; Hakanoglu, C. Facile C−H Bond Cleavage and Deep Oxidation of Propane on a PdO(101) Thin Film. *J. Phys. Chem. C* **2009**, *113* (22), 9773−9782.
(47) Kan, H. H.; Weaver, J. F. A PdO (1 0 1) thin film grown on Pd (1 1 1) in ultrahigh vacuum. *Surf. Sci.* **2008**, *602* (9), L53−L57.
(48) Weaver, J. F. Surface Chemistry of Late Transition Metal Oxides. *Chem. Rev.* **2013**, *113* (6), 4164−4215.
(49) Kinnunen, N. M.; Hirvi, J. T.; Suvanto, M.; Pakkanen, T. A. Role of the Interface between Pd and PdO in Methane Dissociation. *J. Phys. Chem. C* **2011**, *115* (39), 19197−19202.

https://doi.org/10.1021/jacs.4c00312
J. Am. Chem. Soc. 2024, 146, 8641−8649